Fair weather atmospheric charge measurements with a small UAS

Article

Accepted Version

Fair Weather Atmospheric Charge Measurements with a Small UAS

Martin Schön,[a] Keri Anne Nicoll,[b] Yann Georg Büchau,[a] Stefan Chindea,[c] Andreas Platis,[a] Jens Bange,[a]

[a] *Department of Geosciences, Tübingen University, Germany*

[b] *Department of Meteorology, University of Reading, United Kingdom*

[c] *Department of Electronic & Electrical Engineering, University of Bath, United Kingdom*

Corresponding author: Martin Schön, martin.schoen@uni-tuebingen.de

ABSTRACT: Atmospheric electricity measurements made from small unmanned aircraft systems (UAS) are rare but are of increasing interest to the atmospheric science community due to the information that they can provide about aerosol and turbulence characteristics of the atmospheric boundary layer (ABL). Here we present the first analysis of a new data set of space charge and meteorology measurements made from the small, electric, fixed-wing UAS model MASC-3. Two distinct experiments are discussed: (1) Flights past a 99 m metal tower to test the response of the charge sensor to a fixed distortion of the electric field caused by the geometry of the tower. Excellent agreement is found between the charge sensor response from the MASC-3 and modeled electric field around the tower. (2) Vertical profiles up to an altitude of 2500 m to study the evolution of the ABL with the time of day. These flights demonstrated close agreement between the space charge profiles and temperature, relative humidity, and turbulence parameters, as would be expected on a fair-weather day with summertime convection. Maximum values of space charge measured were of order 70 pC m^{-3}, comparable with other measurements in the literature from balloon platforms. These measurements demonstrate the suitability of small UAS for atmospheric electrical measurements, provided that care is taken over the choice of aircraft platform, sensor placement, minimization of electrical interference, and careful choice of the flight path. Such aircraft are typically more cost-effective than manned aircraft and are being increasingly used for atmospheric science purposes.

1. Introduction

Charge is ubiquitous in Earth's atmosphere and is created by galactic cosmic rays from space, as well as surface radioactivity. Vertical separation of this positive and negative charge occurs in thunderstorms and electrified shower clouds, causing Earth's surface to become negatively charged, and the ionosphere (at approx. 70km altitude) positively charged (Wilson 1921). This potential difference generates an atmospheric electric field (E-field), which is present globally, and is directed vertically, such that positive charge flows downwards to Earth. Near the surface, the E-field is approximately -100 V m^{-1} during fair weather conditions, and typically decreases in magnitude with height exponentially (Gish 1944). Clark (1957) devised a rough parameterisation for the decrease of the E-field with height (E_z) in the troposphere in clear air (equation 1).

$$E_z = E_0 \exp^{-az} \tag{1}$$

E_0 is the surface E-field. The reciprocal of the scale height (a = 0.25 km^{-1}), and height (z) are in km. The presence of the atmospheric boundary layer as well as aerosol and cloud layers generally perturb this idealised profile, causing regions of increased E-field from the clear air case (Fig. 1). Measurements of the E-field in fair weather conditions are important for for investigating Earth's global electric circuit, its connection to climate processes and processes in the atmospheric boundary layer (ABL). (Markson and Price 1999; Williams 2009; Rycroft et al. 2012). Atmospheric electrical variables can also provide information on the aerosol content of air (Sagalyn and Faucher 1954), including Saharan dust (Gringel and Muhleisen 1978; Nicoll et al. 2010) and Volcanic ash (Harrison et al. 2010), as well as well as local turbulence characteristics (Markson et al. 1981). This is because the same meteorological processes that transport heat, momentum, moisture, and aerosol within the lower atmosphere also transport charge (Hoppel et al. 1986).

The vertical profile of the atmospheric electric field has been measured since the late 1800s (Tuma 1899), originally using water dropper sensors flown on hot air balloons. Since the early days of these measurements, electric field sensors and airborne platforms have developed substantially, with vertical profiles now typically measured with electric field mills carried by manned aircraft (Winn 1993; Bateman et al. 2007). Measuring the atmospheric E-field using an aicraft is challenging, because every measurement will be influenced by the aircraft's own E-field, which can

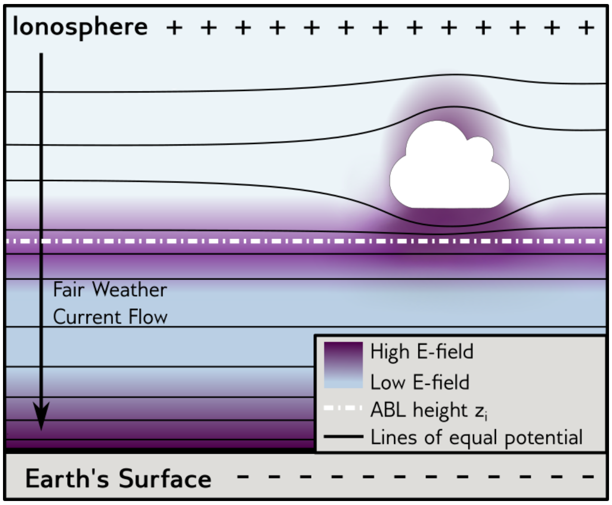

FIG. 1. Schematic of the atmospheric E-field, with the color shading representing the E-field intensity, and the black lines representing equal electric potential. In fair weather conditions, current flows from the positively charged Ionosphere to the Earth's surface. Changes in the atmosphere's resistance, such as the capping inversion of the ABL or clouds create local distortions in the E-field. Distortions in the E-field can also be caused by thermodynamic processes. The E-field close to the surface is approximately -100 V m^{-1} during fair weather conditions, and typically decreases in magnitude with height exponentially (Gish 1944).

lead to substantial measurement errors in regions of high E-fields, such as in convective clouds, thunderstorms, precipitation, or inside dust and aerosol plumes. While early aircraft measurements of E-field were made by using two E-field sensors mounted above and below the wing (Gunn 1947, 1948; Gish and Wait 1950), it was recognized that multiple E-field sensors were required in order to remove the effect of aircraft charge on the measurements. In addition, charging of aircraft surfaces, which influences E-field measurements, can also result from the engine exhaust gases. Subsequent aircraft flights by Clark (1957, 1958) further characterized this distortion of the ambient E-field by the presence of the aircraft ("aircraft reduction factor"). Aircraft measurements of the atmospheric E-field are also affected by the movement of the aircraft itself. Since the total E-field, **E**, is a vector quantity, consisting of components E_x, E_y and E_z, the motion of the aircraft can act to perturb one or more of these E-field components. This effect becomes even more pronounced with large changes in attitude, such as in turns. Winn (1993) discusses the various methods which have been used to correct for the motion of the aircraft. These include using scale models of aircraft (Laroche 1986), electrostatic modeling of the airframe (Mazur et al. 1987), and calibration maneuvering techniques (Winn 1993) to account for pitch and roll motion. More recent aircraft measurements of E-field have attempted to develop procedures to remove all of the above-described effects of the aircraft from the E-field measurements using ever more sophisticated methods. Koshak et al. (1994), Mach and Koshak (2007) and Mach (2015) discuss a detailed inversion matrix technique for calibrating aircraft E-field sensors, as well as a series of aircraft calibration maneuvers required to determine various calibration coefficients. For this technique to work well, several E-field sensors must be mounted on the aircraft (enough to measure at least one component of the E-field), with 5-8 E-field sensors typically used. If the E-field sensors are small (as developed by Bateman et al. 2007), this is possible to implement on a large airframe, but not if payload capacity is limited, such as on small Unmanned Aerial Systems (UAS).

The measurements mentioned above demonstrate that the E-field measured on a moving aircraft platform is often not a direct detection of the ambient E-field, but rather a combination of the aircraft-enhanced ambient field, aircraft motion, charge on the aircraft, and various other effects due to engine exhaust charging, or corona discharge when large E-fields are present. Therefore, it is necessary to remove all perturbations of the natural ambient field caused by the presence of the aircraft to detect the actual ambient field with aircraft measurements.

As opposed to the large aircraft mentioned above, small UAS as a platform for atmospheric electricity measurements are flexible, inexpensive, and allow measurements in conditions that are not possible for crewed aircraft (for example, very close to the ground, near obstacles, or when launching and landing without any infrastructure). Despite the abundant availability of UAS for commercial and hobbyist applications, meteorological measurements from UAS are still relatively rare. Reasons for this include a lack of commercially available, low cost, high accuracy meteorological sensors, a lack of commercially available fixed wing platforms which are suitable for such measurements, complexities of autopilot operation, as well as challenges (both legal and practical) associated with flying at altitudes above standard visual line of sight limits. Technological developments are leading to more meteorological measurements from UAS (e.g., Pinto et al. 2021). Examples of UAS measurements in atmospheric electricity include the development of an "electrostatic autopilot" (Hill 1972, 1982), as well as the miniature E-field sensor measurements of Bateman et al. (2007) on the NASA Altus II UAS. More recently Zhang et al. (2016) instrumented a small UAS with multiple AC electrical potential sensors which utilize the pitch and roll movement of the aircraft to generate voltage differences between pairs of sensors mounted on the pitch and roll axes of the aircraft. Finally, Harrison et al. (2021) described measurements of space charge from a 2 m wingspan fixed UAS through a thin cloud layer.

In this work, we describe two types of measurement, made from a small fixed-wing UAS, model MASC-3. Its small size means that it is not feasible to carry a large number of E-field sensors as per the common approach used on larger aircraft. Instead, we have instrumented the airframe with highly sensitive bespoke miniature space charge sensors (Nicoll and Harrison 2009). Space charge, ρ, is the difference between positive and negative charge per unit volume, and is related to the divergence of the E-field, by Gauss' law (equation 2).

$$\nabla \cdot \mathbf{E} = \frac{\rho}{\epsilon_0} \tag{2}$$

where ϵ_0 is the permittivity of free space, and $\mathbf{E}$ is a three-dimensional vector of orthogonal components E_x, E_y and E_z. When measuring space charge in the atmospheric boundary layer (ABL), we are concerned with the vertical profile of ρ which can be derived by considering the vertical component of the electric field, E_z (provided that variations in E_x and E_y are smaller than those in E_z, as is often the case in fair-weather conditions). Thus, ρ can be derived by equation 3, where z is the vertical coordinate, and the positive z direction is upwards.

$$\rho = \epsilon_0 \frac{dE_z}{dz} \tag{3}$$

We performed two types of measurements at the MOL-RAO (Meteorological Observatory Lindenberg, Richard-Aßmann Observatory) of the German Meteorological Service (Deutscher Wetterdienst, DWD) in Germany. First, the validity of the charge sensor is tested by detecting a known distortion in the E-field caused by a 99 m metal tower, and comparing the measurement results with a model (Section 3a). Second, we describe new measurements of vertical profiles of space charge. Flights took place only during fair weather conditions, which minimized the effect of charge build-up on the airframe or corona discharge issues; and the lack of aircraft exhaust from the UAS (which uses an entirely electric propulsion system) means that there is no aircraft charging from emissions, unlike on a manned aircraft.

The instrumentation and aircraft platform are described in section 2a, and the flight location and experimental setup are described in section 2b. Sections 2c and 2d investigate the effect of aircraft movement on the charge measurements, and the development of a technique to remove it. While section 3a serves as a validation for the charge sensor by comparing the measurement to a known perturbation in the E-field caused by a metal tower, section 3b demonstrates the effectiveness of the charge sensor at measuring natural variations in space charge by describing vertical profiles of space charge and meteorological measurements in a series of flights within the ABL at different hours. A discussion section is provided in section 4 and conclusions in section 5.

2. Methods

a. UAS platform

The UAS flights described in this paper were performed by the MASC-3 (Multiple Purpose Airborne Sensor System), a 4 m wingspan fixed-wing UAS for atmospheric measurements (Wildmann et al. 2014a; Mauz et al. 2019; Rautenberg et al. 2019) (Table 1, Fig. 2 b). MASC-3 carries a sensor payload of up to 1.8 kg for measuring the three-dimensional wind vector and air temperature with a temporal resolution of up to 30 Hz, using a five-hole probe and a fine-wire platinum thermometer (Wildmann et al. 2013, 2014b) in combination with an IMU (Inertial Measurement Unit). In addition, the relative humidity is measured using a slower digital temperature and humidity sensor. Data is logged and saved on board the aircraft at a sampling rate of 100 Hz (Rautenberg et al. 2019). MASC-3 is controlled by an autopilot, so it can repeat measurement patterns reliably. It performs all measurements during straight flight sections, with a constant airspeed of 18.5 m s^{-1}, and with the autopilot stabilising the aircraft's attitude along the roll, yaw and pitch axes (Fig. 2). Changes in flight direction are achieved by a change in the aircraft's attitude, mainly along the roll and yaw axes. However, turbulence can also change the aircraft's attitude during a straight section, with the autopilot working against these movements to stabilize the aircraft.

In addition to the standard sensor payload, two pods carrying charge sensors are attached to the wings, 1 m from the fuselage of the aircraft (Fig. 2). The charge sensors are similar to those described in Nicoll and Harrison (2009) and Nicoll (2013). They consist of a small (12 mm) spherical sensing electrode connected to an electrometer circuit. The sensors measure the rate of voltage change on the electrode, where the voltage change is due to the current flow between

TABLE 1. Technical Data for the MASC-3 UAS with Charge Measurement Pods attached.

Wingspan	4 m
Takeoff Weight	8 kg
Payload	1.8 kg
Max. Endurance	1.5 hours
Cruising/Measurement Airspeed	18.5 m s^{-1}
Service Ceiling	4500 m AGL
Propulsion	Electric (pusher configuration)
Autopilot System	Cube, Arduplane firmware
Fuselage Material	Glass Fiber Composite
Wing Material	Carbon Fiber Composite

the atmosphere and the electrode due to the sensor's motion through an E-field. The circuit uses a current to voltage converter with a T-network of resistors to minimize the need for high value resistors (as discussed in Nicoll (2013). Details of the method used to convert the measured charge sensor current to space charge are described in section 3e.

MASC-3 carries four of these charge sensors, with one "normal" range sensor and one "sensitive" sensor on each wing. The "sensitive" sensor provides an increased resolution, while the "normal" sensor has a wider range and is therefore more robust against saturation when measuring a strong signal. Both for the tower fly by (Section 3a) and the vertical profiles of the ABL (Section 3b) is better suited. Generally, the selection of the sensor sensitivity is done in post processing based on the range of the captured signal.

The sensors are mounted in the front of the pods so that the electrodes are about 20 cm away from the leading edge of the wing. The front part of the pods is wrapped with conductive copper foil. This reduces the potential influence of static charge build-up on the charge measurement. Both pods include a microcontroller-based logging system, which captures the analog 0-5 V signal from the charge sensors with a resolution of 14 bits and a sampling rate of 100 Hz directly to an SD-Card inside the pod. The timestamp of the charge sensor data and the rest of the sensor system are referenced to GPS time for synchronization.

b. Site Description and Experimental Setup

The UAS flights described here took place at the German Meteorological Service (DWD) MOL-RAO (Meteorological Observatory Lindenberg, Richard-Aßmann Observatory), about 60 km

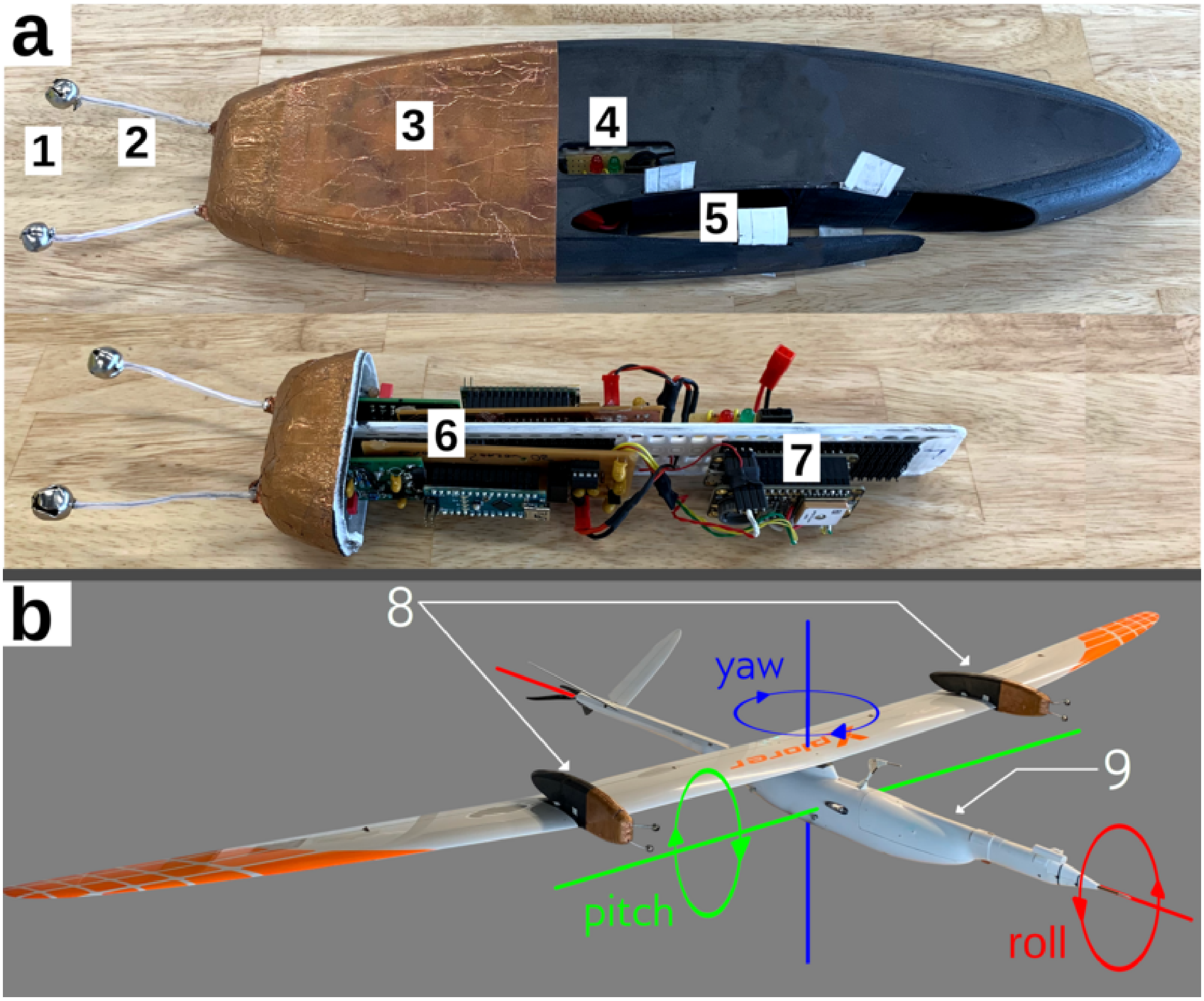

FIG. 2. a: Charge sensor pod for MASC-3. Sensing electrode (1), plastic-covered connector to sensor board (2), shell painted with conductive graphite paint, front section covered in conductive copper foil (3), status lights (4), wing mount (5), sensor board, and an analog-digital converter (6), Adafruit Feather microcontroller for logging and GPS antenna for creating timestamps (7).
b: MASC-3 with charge sensor pods attached. The charge sensor pods (8) are covered in conductive copper foil to reduce the influence of static charge around the non-conductive surface of the wings. The sensor payload is in the front for measuring the wind vector, temperature, and humidity (9). The three dimensions of movement (yaw, pitch, roll) of MASC-3 are measured by the IMU mounted in the sensor payload.

southeast of Berlin (Fig. 3). Flights were performed during June 2021 by the Environmental Physics Workgroup of the University of Tübingen. The MOL-RAO site also includes a 99 m high

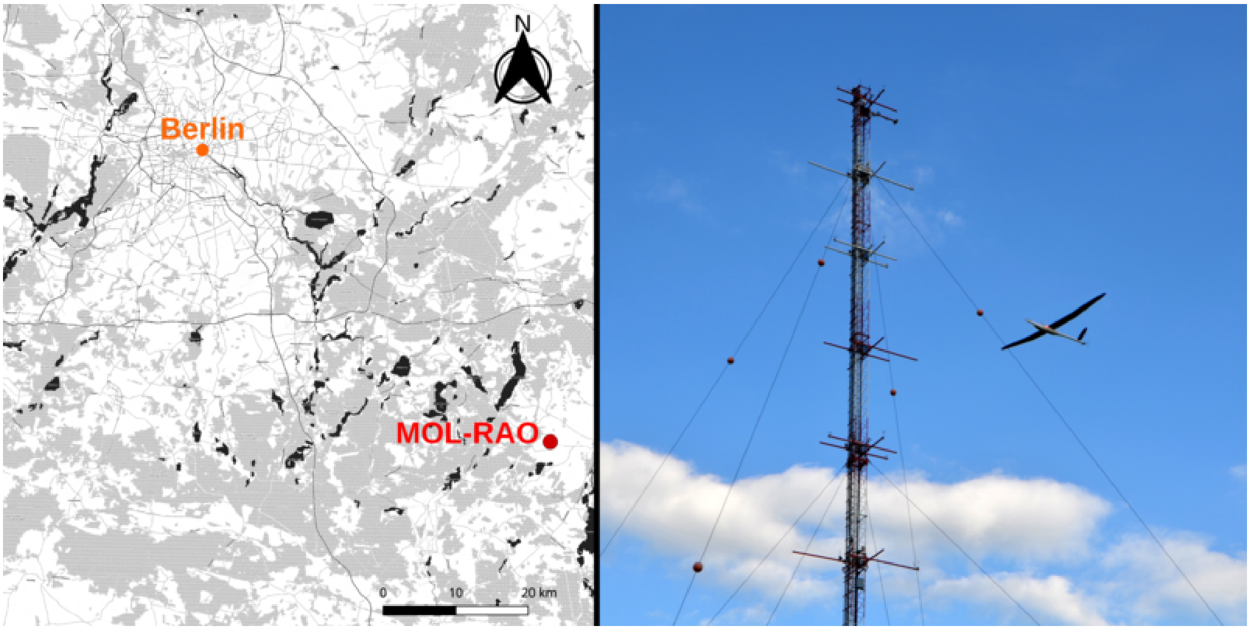

Fig. 3. Location of the MOL-RAO meteorological tower, MASC-3 passing the tower during a measurement flight.

meteorological measurement mast, located at 52.1665° E 14.1222° N, 73 m above sea level (ASL). The site is flat, with a maximum variation in terrain elevation of 10 m within a 5 km radius.

In order to test the response of the charge sensors on the UAS, two types of measurement flight were conducted. To validate the MASC-3 space charge measurement, an experiment was designed in which MASC-3 flies through a known distortion in the E-field, caused by the measurement tower. To establish this reference for the measurements of MASC-3, the E-field around the tower was modeled in the COMSOL physics software (electrostatics package) (COMSOL 2021). Like any large metal object, the tower perturbs the E-field around it, which causes changes in the charge sensor output as the MASC-3 flies past it. The space charge calculated from the charge sensor output is then compared to the divergence of the modeled E-field. (section 3a).

The second pattern involved vertical profiles, where MASC-3 climbs to 2500 m above ground with a constant vertical velocity of 1.5 m s^{-1} in a series of 1.5 km long sections (Fig. 4). From these sections, only a central section of 800 m length is used for analysis to further reduce the influence of the turns at the end of the sections. This flight pattern aimed to measure natural perturbations in

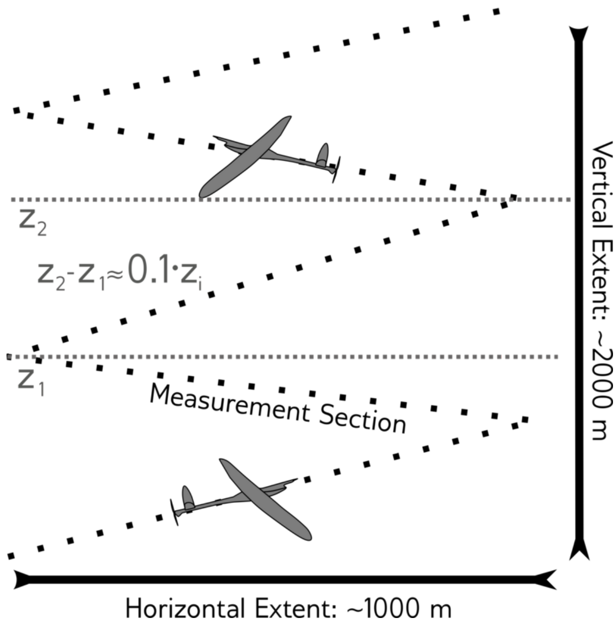

FIG. 4. MASC-3 flight path for the vertical profile flights. The profile is divided into several sections. Each pair of these sections (upwind and downwind) covers a height of 10% of the boundary layer height $0.1 \cdot z_i$.The maximum altitude for each flight varies, dependent on weather situation and airspace restrictions, see Tab. 2.

the E-field caused by variation of the ABL in fair weather and is discussed in section 3b. Of this pattern, a total of 13 flights were conducted (as shown in Table 2).

To perform these measurement flights beyond the pilot's visual line of sight (BVLOS) at these altitudes, special permits are required in most countries. In the case presented here, the flights were made possible by the establishment of a no-fly zone and subsequent permits for BVLOS UAS flights. In the EU, these permits are not necessarily expensive, but it is important to contact the relevant authorities at an early stage, as such procedures may take a long time and be quite extensive, depending on the risk assessment of the planned flights.

c. Effect of UAS movement on charge measurements

Aircraft movement is well known to affect E-field measurements made from manned aircraft platforms (Winn 1993; Mach and Koshak 2007). Winn (1993) suggest that the total charge, Q, induced on an E-field sensor electrode is a linear sum of the contributions of the E-field in the x, y and z directions (E_x,E_y,E_z) as well as the charge on the aircraft Q_A (equation 4)

TABLE 2. Overview of the MASC-3 measurement flights with charge sensor pods performed in May and June 2021. The tower fly by flight (discussed in section 3a), and vertical profiles discussed in section 3b are highlighted in bold. Time is local time (LT): Central European Summer Time

Flight No.	Date	Time (LT - CEST)	Type	Max. Altitude (m AGL)
calibration	**03.05.2021**	**14:00 - 14:23**	**Horizontal Legs**	**100**
1	09.06.2021	15:53 - 17:00	Vertical Profile	2200
2	10.06.2021	09:14 - 10:32	Vertical Profile	700
3	10.06.2021	11:24 - 12:33	Vertical Profile	1700
4	10.06.2021	14:13 - 15:30	Vertical Profile	2000
5	10.06.2021	15:56 - 16:45	Vertical Profile	2000
6	13.06.2021	19:02 - 20:00	Vertical Profile	2100
7	**14.06.2021**	**07:05 - 08:08**	**Vertical Profile**	**2100**
8	**14.06.2021**	**09:03 - 10:15**	**Vertical Profile**	**1600**
9	**14.06.2021**	**13:57 - 15:01**	**Vertical Profile**	**1780**
10	14.06.2021	16:57 - 17:45	Vertical Profile	1750
11	**16.06.2021**	**20:16 - 21:30**	**Tower fly by**	**150**
12	17.06.2021	09:53 - 11:30	Vertical Profile	2360
13	17.06.2021	14:00 - 15:00	Vertical Profile	2500
14	17.06.2021	16:53 - 18:30	Vertical Profile	2300

$$Q = aE_x + bE_y + cE_z + Q_A \tag{4}$$

(where a, b, c are coefficients specific to the aircraft). Aircraft charging is most likely to occur when flying through layers of droplets (e.g. clouds) or particles (dust, sand, smoke, ash). By flying in only fair weather conditions with no clouds or haze layers, the effects of Q_A are minimized so that this term becomes negligible.

The E_x and E_y terms will likely be most sensitive to pitch and roll maneuvers from the UAS, and the E_z term will vary with UAS altitude as the aircraft climbs or descends. The degree to which the E-field measurement is affected by pitch and roll movements depends on the placement of the sensors with respect to the various axes of rotation of the UAS. For the MASC-3, the charge sensor pods were deliberately mounted on the wings, relatively close to the aircraft's main body (1 m distance), rather than nearer the wingtips. Placement towards the end of the wings would result in a much larger sensitivity to roll maneuvers due to the larger angles through which the UAS wings move.

The dependence of the charge sensors on the UAS movement was investigated by cross-correlating the charge sensor voltage output with all MASC-3 flight parameters, including roll angle, roll velocity, pitch velocity, and yaw velocity (aircraft axes are depicted in Fig. 2b), for multiple measurement flights. The result of this was an observed high correlation between charge sensor output and roll velocity (with a maximum correlation coefficient between 0.6 and 0.9, at a lag between 0.1 s and 0.3 s). A less significant correlation with pitch velocity was observed, with typical correlation coefficients between 0.2 and 0.4. The high correlation with roll velocity is likely due to the placement of the charge sensors. Since the sensors are mounted on the wings, 1 m away from the aircraft's axis of rotation, a slight roll movement is translated by the leverage into a fast absolute movement of the charge sensor, while the sensor's movement is minimal during a pitch movement, since it is only about 20 cm away from the pitch axis. Correlation to movement around the yaw axis is not detected, and MASC-3 is generally more stable in the yaw axis than in the roll or pitch axes.

To further investigate the sensitivity of the charge sensors to changes in the UAS roll velocity, calibration maneuvers were devised in which the human pilot deliberately performed a slow rolling motion of the aircraft. This is demonstrated in Fig. 5. A strong correlation is seen between the charge sensor output and the roll velocity of the MASC-3. Fig. 5 shows the data for the sensor located on the right wing (which is positively correlated with roll velocity). The left wing charge sensor shows an equal but opposite (i.e., negative) correlation with roll velocity, as expected (not shown here). To minimize the influence of the roll maneuvers of MASC-3 on the charge sensor output, the measurement flights were carried out as a series of straight, 1 km long sections, which are called measurement legs (for straight and level sections) or measurement sections (for straight sections including an ascent/descent) in the remainder of this study. Only these sections are taken into account in the data analysis sections of 3a and 3b, and data from the turns are discarded (as the charge sensor often saturates due to the high roll velocities from the UAS). For sections with roll velocities below 0.2 rad s^{-1}, the correlation coefficient of the charge sensor and the roll velocity drops below 0.5. Although this approach minimizes the influence of the roll velocity on the charge sensor data, it does not remove it completely. For example, the roll influence is visible in straight measurement sections when the MASC-3 autopilot performs roll movements to compensate for atmospheric turbulence. This may be a problem in turbulent conditions, such as a convective ABL,

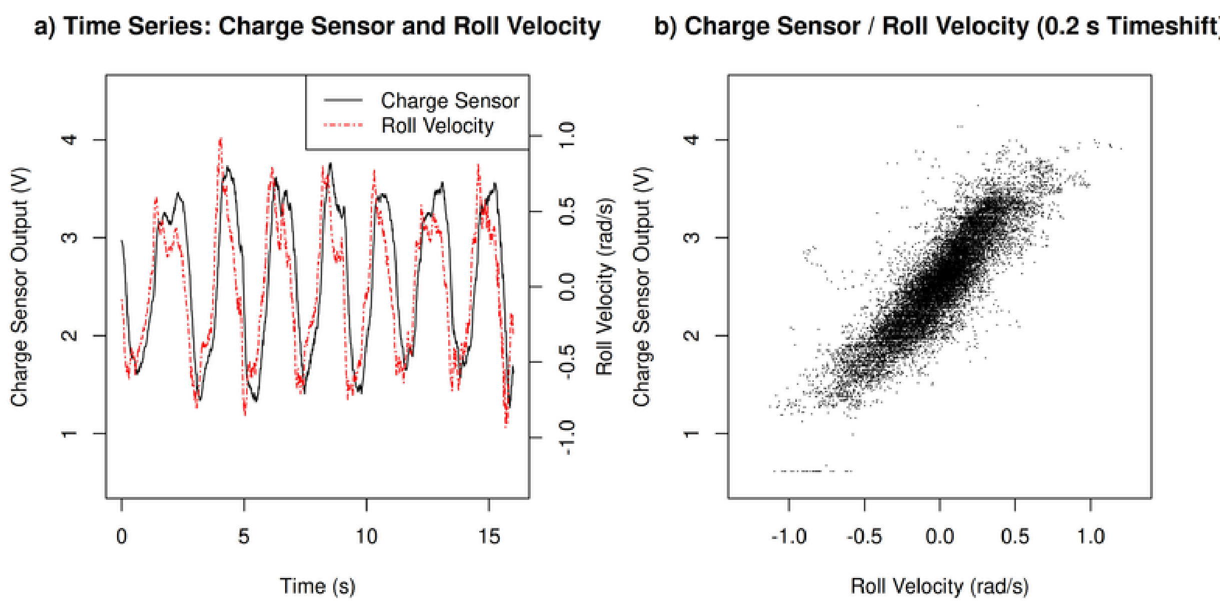

FIG. 5. a: Time Series of charge sensor signal (black) and roll velocity (red) for a calibration leg with an oscillating roll movement generated by the pilot. The time shift between roll movement and charge sensor response is approx. 0.2 s. b: Relationship between roll speed and charge sensor output for an entire flight with pilot-generated roll movement, created from 108 s of data sampled with 100 Hz. Roll Velocity data is timeshifted by 0.2 s to account for the lag in the charge sensor response.

where a charge signal with a higher amplitude is measured due to the stronger roll movements. Therefore, a roll velocity correction to the charge sensor data is required to interpret the charge sensor measurements.

d. Exponential Smoothing Correction Method

With the roll velocity and charge measurements recorded during the calibration flight (Table 2), a correction method for the charge measurements can be implemented. This method uses the roll velocity to generate a correction signal that is subtracted from the charge sensor signal to eliminate roll influence as much as possible. When comparing the charge sensor output signal (0 - 5 V), U_{raw} and roll velocity signal v_{roll}, a lag between the two signals is apparent (typically 0.1 - 0.3 s, depending on the sensor). The charge sensors slower response time causes its response to resemble a smoothed and lagged version of the roll velocity signal. A simple method of modeling this response is by filtering an appropriately normalized roll velocity signal $v_{\text{roll,norm}}$ with an exponentially weighted moving average (EWMA) (Holt 2004). $v_{\text{roll,norm}}$ is obtained using the anomalies of roll velocity during a calibration leg, $v'_{\text{roll,calib}}$, which are scaled to have the same signal energy as the charge signal anomalies $U'_{\text{raw,calib}}$ (Guido 2016) and then shifted to match the charge signal mean (equation 5).

$$v_{\text{roll,norm}} = \sqrt{\frac{\int \left|U'_{\text{raw,calib}}\right|^2 dt}{\int \left|v'_{\text{roll,calib}}\right|^2 dt}} \cdot v'_{\text{roll}} + \overline{U_{\text{raw}}} \tag{5}$$

Applying the EMWA filter on the normalized roll velocity $v_{\text{roll,norm}}$ yields a correction signal s_{corr} which closely models the roll velocity's influence on the charge signal (equation 6).

$$s_{\text{corr}} = v_{\text{roll,norm}} * k_{\text{exp}}(\tau) \tag{6}$$

To find the kernel $k_{\text{exp}}(\tau)$ for the EMWA filter, we use the charge sensor's time-constant τ. Determining τ is possible by minimizing a cost function representing the deviation between $s_{\text{corr}}(\tau)$ and U_{raw} in a flight leg with reasonably strong, controlled, pilot-induced roll movements where no external influence on the charge sensor is expected (Fig. 6). The roll velocity during this calibration must be high enough to produce a clear signal in the charge sensor but low enough not to cause saturation of the sensor. We used the root-mean-squared-error (RMSE) as a cost function. Subtracting s_{corr} from the raw charge signal c_{raw} results in a corrected charge signal c_{corr} with reduced roll velocity influence (equation 7).

$$U_{\text{corr}} = U_{\text{raw}} - s_{\text{corr}} \tag{7}$$

The results of this correction method are shown in Fig. 6 for both a calibration leg and a normal straight leg during a measurement flight. Our proposed correction method greatly reduces the roll velocity's influence on the charge sensor signal. For the calibration period (Fig. 6a), the signal energy of the erroneously oscillating charge signal is reduced by 85 percent. In a straight leg of the same flight, numerous roll-induced peaks in the charge measurement are diminished, leaving a cleaner and easier to interpret time series (Fig. 6b). For legs and flight sections during the

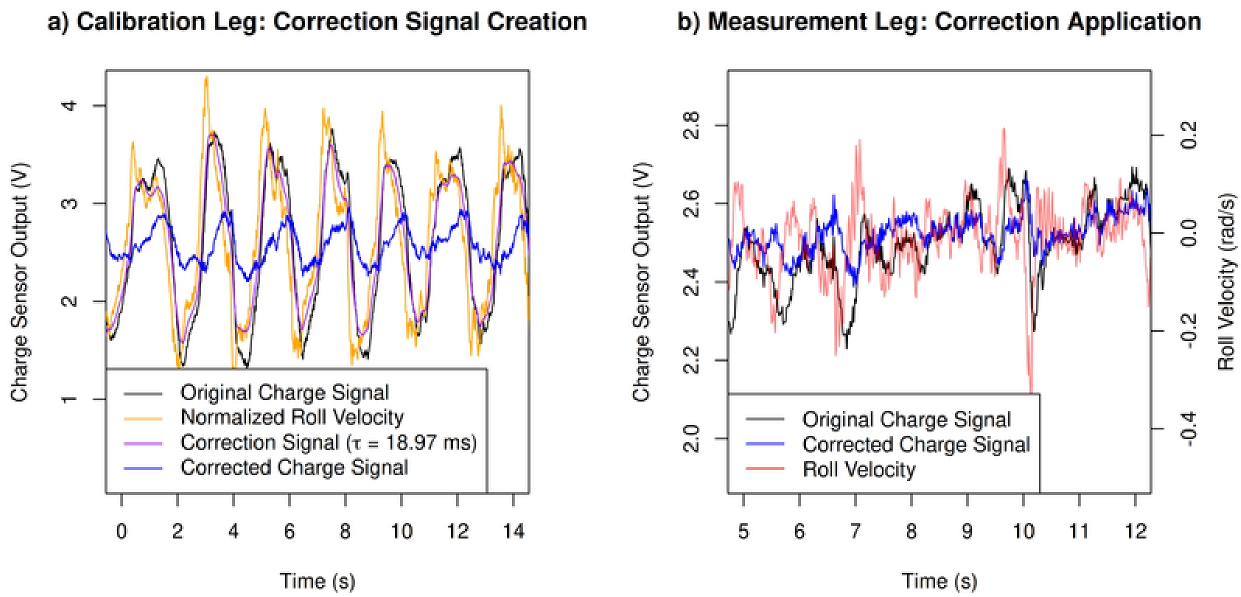

FIG. 6. a: Calibration leg containing a rolling motion created by the pilot to determine the charge signal's time constant. The normalized roll velocity ($v_{\mathrm{roll,norm}}$ orange) is filtered with an exponentially weighted moving average (EMWA) to match the original charge signal (U_{raw}, black) as closely as possible. The resulting optimized signal (s_{corr}, purple) is then subtracted from the charge signal to obtain a corrected charge signal (U_{corr}, blue). The optimization of the EMWA kernel yields a time constant τ of 18.97 ms for the charge sensor signal.
b: The parameters calculated in the calibration leg are used to filter the influence of roll velocity (red) on the charge measurement (black) in a measurement leg of the same flight as the calibration leg. The filtered signal (blue) shows a reduced influence of the rolling motion. Note the lower amplitude of both charge and roll velocity during measurement legs without intentionally created rolling motion.

measurement flights performed in Lindenberg (Table 2), the correlation coefficients between v_{roll} and charge are reduced from 0.5 - 0.6 to ≈0.4 by implementing the filtering approach.

e. Space Charge Calculation

The space charge measured by the charge sensor is derived using a series of procedures detailed below. Firstly, the current I_i is calculated from the corrected (as described in section d) 0-5 V output of the sensor U_{corr}, as the sensor is essentially a displacement current sensor, which produces a current in response to a varying E-field. (equation 8).

$$I_i = \frac{-\left(U_{\mathrm{corr}} - U_{\mathrm{bg}}\right)}{R_{\mathrm{sensor}}} \tag{8}$$

The value of the gain resistor is $R_{\mathrm{sensor}} = 2.4 \cdot 10^{11}\Omega$, and U_{bg} is the background voltage of the charge sensor (this is typically 2.55 V for the flights discussed on June 14).

Secondly, I_i, is then converted to space charge ρ (equation 9), by dividing I_i by the vertical speed of MASC-3 w_{MASC} multiplied with the effective area term of the sensor $A_{\mathrm{eff}} = 0.02\ \mathrm{m}^2$, derived from experimental calibration (Nicoll and Harrison 2016).

$$\rho = \frac{I_i}{A_{\mathrm{eff}}} \cdot w_{\mathrm{MASC}} \tag{9}$$

It is assumed that in fair weather conditions, any changes in space charge in the horizontal will be minimal and that changes in the vertical will dominate the space charge measurement. For vertical profiles of the ABL, we therefore use the vertical speed w_{MASC} measured by the IMU aboard MASC-3 (in m s^{-1}, positive upwards). For the flights presented here, this is $w_{\mathrm{MASC}} \approx 1.5$ m s^{-1}. Finally, only the absolute value of space charge is used here as discussed in Nicoll et al. (2018).

3. Results

a. Tower fly by

To validate the response of the charge sensor to changes in the ambient E-field on a moving UAS platform, a series of flights were performed next to a 99 m meteorological measurement tower. This was located at the MOL-RAO (Meteorological Observatory Lindenberg - Richard-Aßmann Observatory) of the German Meteorological Service (Deutscher Wetterdienst, DWD) in the area of Brandenburg, Germany, 60 km southeast from Berlin. The structure of the tower consists of a 99 m metal mast, supported by four guy ropes (which extend diagonally 45 m from the center of the tower), as shown in Fig. 7. It is well understood that the existence of such a tower will distort the ambient atmospheric E-field around it due to the enhanced geometry of the structure. As such, flying the UAS past the tower at various distances and altitudes provides a control experiment testing the response of the charge sensor to the variations in the E-field caused by the tower. Fig. 7 shows the various flight legs performed with the UAS at four altitudes (40 m, 60 m, 80 m, and 100 m). Per altitude, measurement legs were flown as repeated 400 m straight legs past the tower at

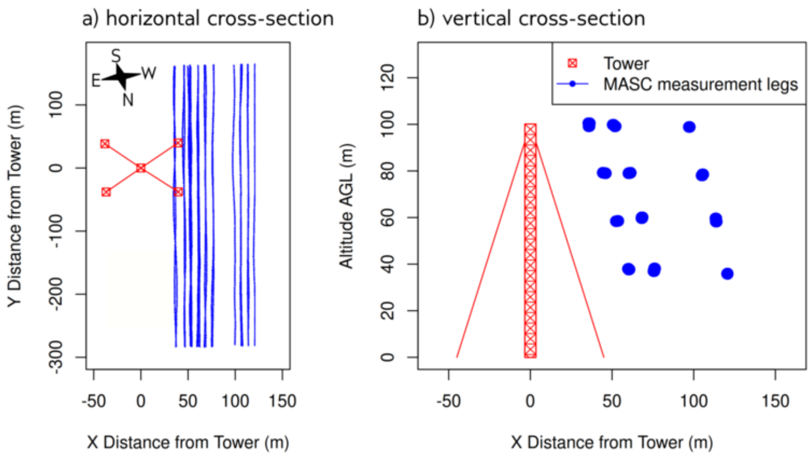

FIG. 7. Top view and Profile of the meteorological Tower at Falkenberg including its guy ropes (red) and the MASC-3 measurement legs next to the tower (blue). The coordinate system is relative to the position of the tower.

three different horizontal distances (coordinate x). For the lowest altitude of 40 m, these distances are 60 m, 80 m, and 120 m from the center of the tower. In an attempt to follow the angle of the guy ropes, the horizontal distance from the tower became smaller with altitude (as shown in Fig. 7b), but always maintained a consistent (closest) distance of 40 m from the guy ropes.

To model the distortion of the E-field around the tower, the COMSOL physics software was used. This solves Gauss' Law for the electric field using the scalar electric potential as the dependent variable. The tower was modeled as a 99 m tall, 5 m diameter metal conductor, with four diagonal conductive guy ropes, all of which are earthed. As an approximation of the ambient fair-weather atmospheric E-field, the E-field is generated by a parallel plate capacitor setup with a vertical separation distance between the plates of 300 m. The capacitor is cylindrical (to enable axial symmetry), and the top plate is at 30,000 V, in effect generating a uniform E-field of 100 V m^{-1}. Fig. 8 shows the modeled E-field around the tower through a cut-plane at 45 degrees to the x axis (i.e., the guy ropes appear on either side of the tower as in Fig. 7b). It is seen that the intensity of the E-field drops significantly in between 0 m and 50 m distance from the tower and varies with altitude. The equipotential lines are highly curved close to the tower and guy ropes, but this decreases with horizontal distance and is negligible at distances of two to three times the towers height (i.e., beyond

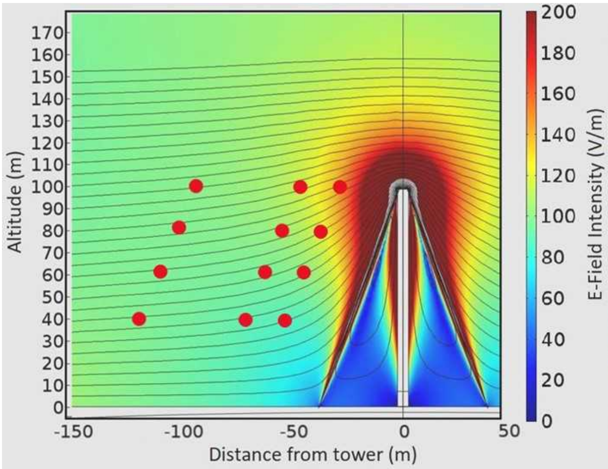

FIG. 8. COMSOL modelling of distortion of E-field around a 99 m mast. Coloured contours show modelled E-field and black lines are lines of equal electric potential at 20 m intervals (from 20 m - 100 m). Red circles denote the location of the UAS flight legs as in Fig. 7.

200 m). It should be noted that the model of the tower is very much an approximation of the real tower, hence the COMSOL simulation will not capture any effects of corona discharge, which may affect the E-field and space charge around sharp points such as crossbeams on the tower. The fair weather conditions (and hence small ambient atmospheric E-fields) during the flights should minimise this issue.

An example of the typical response of the charge sensor as the UAS flies past the tower is shown in Fig. 9. This illustrates that the charge sensor voltage is relatively stable on approach to the tower (i.e., left-hand side of the plot). When the UAS gets within 50 m (coordinate y as shown in Fig. 8b) of the tower, the charge sensor voltage decreases and reaches a minimum at the closest distance to the tower. As the UAS continues to fly past the tower, the charge sensor voltage increases and returns to approximately its original value. Although the example shown in Fig. 9 is for the flight leg flown at 40 m horizontal x distance from the tower at an altitude of 80 m AGL, all of the flight legs in Fig. 7 show a similar type of response for the charge sensor, just with varying values of voltage change. To calculate the space charge ρ from this signal, equation 9 has to modified for this experiment to use the velocity along the flight path v instead of the vertical velocity w, since the E-field mainly changes along the flight path, as the aircraft passes the influence of the tower.

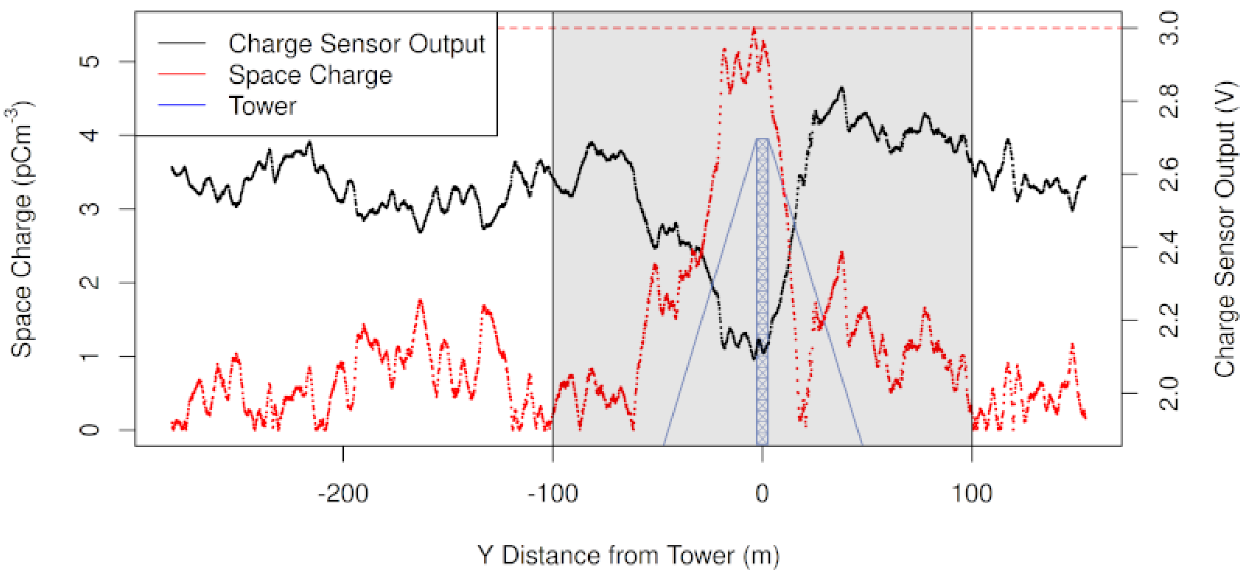

FIG. 9. The typical response of the charge sensor (black) during a measurement leg at an altitude of 80 m AGL with the closest distance of 40 m to the tower. The local minimum of the waveform is typically around the point closest to the tower, the local maximum within 100 m after passing the tower. Space charge is calculated from this measurement leg (red), with the maximum space charge within a ± 100 m distance along the y coordinate along the tower (red dashed line).

As such, we calculate the maximum space charge ρ_{max} for each flight leg within a coordinate y of ± 100 m from the center of the tower. This calculation is made for each of the 12 flight legs (i.e., straight and level flight sections) at different x distances and altitudes from the tower as shown in Fig. 8b. ρ_{max} for each leg are shown as black crosses in Fig. 10, illustrating an exponential decrease in ρ with x distance from the tower.

As described in eq. 3, ρ is directly related to the divergence of the E-field along the component along which the E-field is changing most. For the E-field around the tower, we assume this component to be the distance to the tower r. Therefore, a qualitative comparison between the divergence of the simulated E-field with respect to the distance to the tower, $\frac{dE_{\mathrm{sim}}}{dr}$, and the measured space charge ρ is possible. Both $\frac{dE_{\mathrm{sim}}}{dr}$ and ρ show an exponential decrease with increasing r (Fig. 10). Exponential fits of the form $y(x) = y_f + (y_0 - y_f) \cdot e^{-\alpha \cdot x}$ to the measured and modeled data demonstrate that the values of the coefficients of the exponents, α, are similar between the

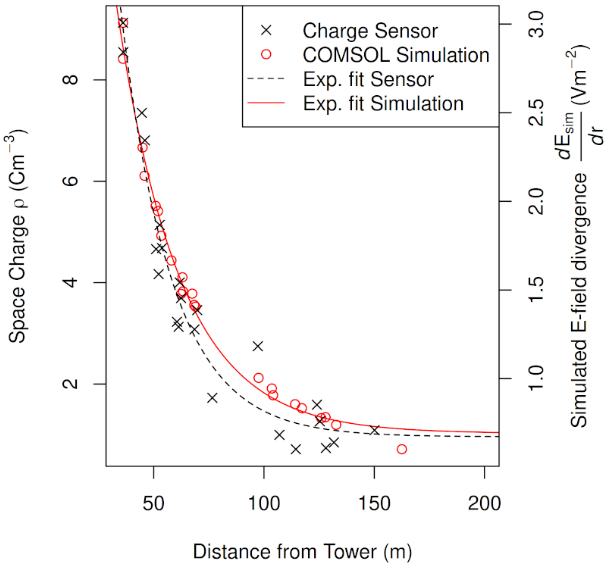

FIG. 10. Comparison of E-field divergence in relation to the distance to the tower $\frac{dE_{\mathrm{sim}}}{dr}$ from COMSOL Simulation with charge sensor space charge ρ in relation to the lateral distance from the tower. Exponential fit is of the form $y(x) = y_f + (y_0 - y_f) \cdot e^{-\alpha \cdot x}$, $\alpha = 0.043$ km^{-1} for the measured data, $\alpha = 0.035$ km^{-1} for the simulation.

two fits (0.043 km^{-1} for the measured data and 0.035 km^{-1} for the modeled data). This gives confidence that the charge sensor responds to the E-field distortion produced by the tower in an expected way.

b. Vertical Profiles

To investigate the response of the charge sensor mounted on MASC-3 to natural variations in E-field, vertical profiles were performed throughout the ABL at the MOL-RAO. Of the 13 vertical profiles mentioned in Tab. 2, three of these are selected here for detailed analysis. These flights were performed on the same day (14 June 2021) to study the evolution of the ABL, with flights occurring at 0700, 0900, and 1400 LT (local time, CEST). The weather conditions were dominated by fair weather, with relatively high pressure (1016-1011 hPa). Scattered clouds in the early morning dissipated shortly after sunrise, followed by cloudless conditions for the remainder of the day. The maximum temperature was 25° C, and near-surface wind speed was very low throughout the day, at 1-2 m s^{-1}. Fig. 11 shows vertical profiles of the meteorological variables measured during June 14 from MASC-3 (including temperature, relative humidity, wind speed, k), and the absolute value of space charge derived from the normal charge sensor on the right wing.

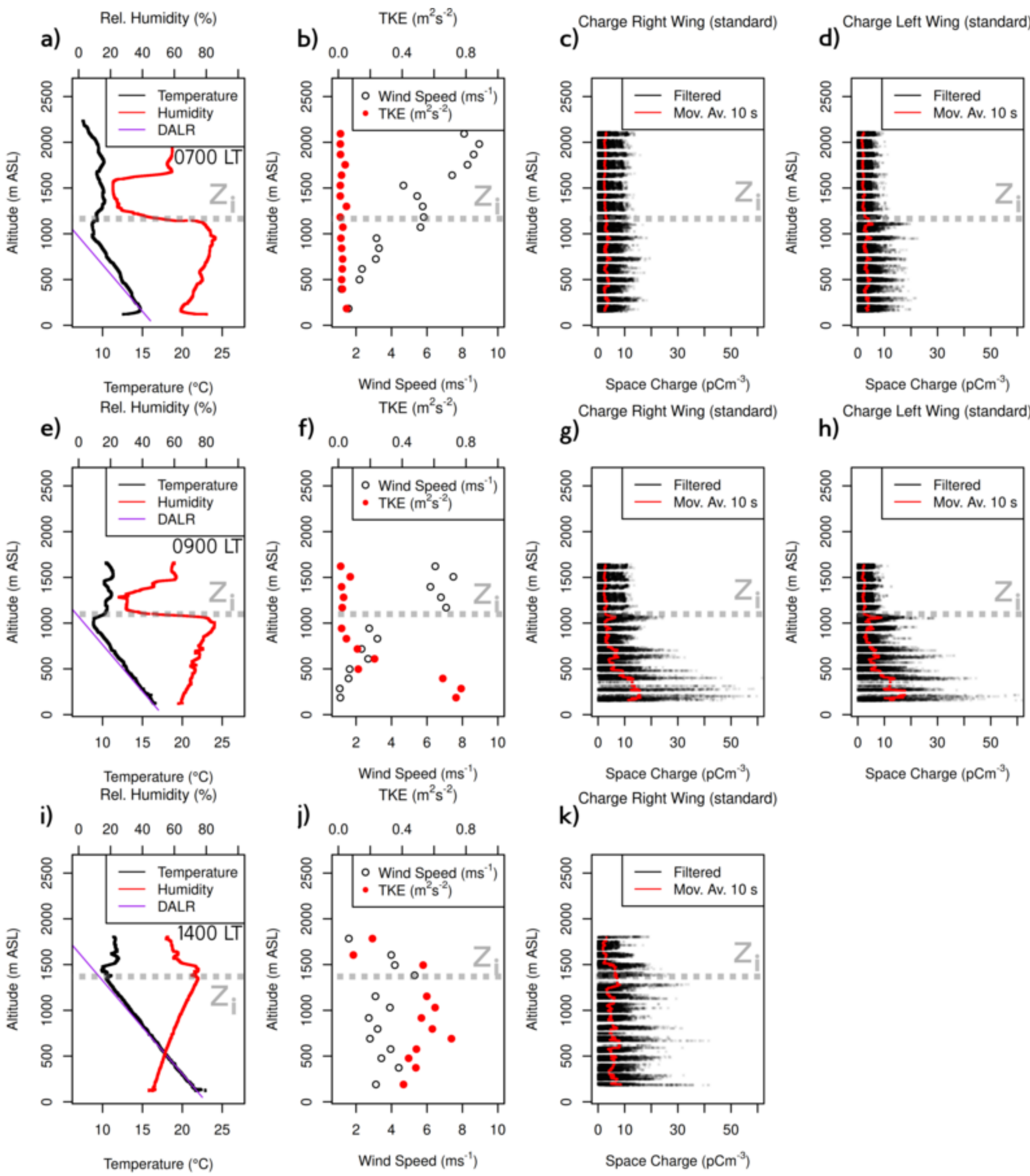

FIG. 11. MASC-3 Vertical Profiles showing the ABL development on 14 June 2021. The altitude of the capping inversion z_i is marked by a dashed grey line. Time information is in Local Time (LT, CEST). Wind Speed and TKE k (as described in appendix a) is per 800 m measurement section, space charge is calculated according to the method in section 2e, with each black dot representing a space charge measurement at 100 Hz sampling rate. The red line in the space charge profiles shows a 10 second moving average of space charge. For the flights at 0700 LT and 0900 LT, the space charge is calculated from the "standard" range sensors on the left and right wing, for the flight at 1400 LT, the left wing sensor malfunctioned, so only the right wing sensor is shown.

Starting with the first vertical profile at 0700 LT, the temperature profile is stable, with an inversion at 190 m ASL (120 m AGL) (Fig. 11a). This is a manifestation of the nocturnal boundary layer from the previous night. The wind speed (Fig. 11b) increases almost linearly up to the altitude of the capping inversion (z_i). Examination of the space charge profile (Fig. 11c, d) shows little variation in space charge with height and values typically up to 20 pC m^{-3}. There is a hint of slightly larger values of space charge within the ABL, but this is not significant. By the time of the second flight at 0900 LT (Fig. 11e), the morning transition eroded the ground-based temperature inversion, and the temperature decreases almost linearly with height, following the dry adiabatic lapse rate (DALR). The temperature inversion at 1 km has strengthened. Fig. 11f shows that k also starts to increase within the ABL, signifying that convective processes are becoming dominant. Evidence of this is also present in the space charge profile (Fig. 11g, h), which shows much more variability than the previous flight, with three distinct layers forming at approximately 0-400 m, 600-700 m, and 800-1000 m. Values of up to 70 pC m^{-3} are now observed. The space charge correlates with k and is significantly stronger within the ABL than above, demonstrating the strong link between space charge and turbulent processes and that the space charge is prevented from mixing to higher altitudes by the capping inversion. By the time of the final flight at 1400 LT, the ABL is well mixed, with the height of z_i increasing to 1.5 km, and the k values approximately constant with height to this altitude. The distinct layers of space charge from the 0900 LT profile have been replaced by a profile that shows high variability with values of up to 40 pC m^{-3} over the complete profile up to the maximum flight altitude of 1.5 km (Fig. 11k).

4. Discussion

This paper addresses three aspects to test whether a small UAS is a suitable platform for atmospheric electricity measurements.

First, the influence of aircraft movement on the E-field around an aircraft, which is a phenomenon described in depth in the literature (Clark 1957, 1958; Winn 1993; Laroche 1986; Mazur et al. 1987; Winn 1993; Koshak et al. 1994; Mach and Koshak 2007; Mach 2015) has to be evaluated, and the influence of the aircraft on the charge sensor signal must be isolated as far as possible. MASC-3 is a pusher aircraft, with the propeller located at the back of the UAS, more than 1 m distant from any of the sensors. This ensures minimal disruption to the charge sensors from the propulsion system. The design of the sensor pods also helps reducing interference to the charge sensors. The geometry of the pods was specially designed to minimize turbulent airflow around the sensors, and mounting them tens of centimeters in front of the wings also assists with this. The placement of the pods, relatively close to the center of the aircraft body, is a compromise between minimizing the effect of roll velocity on the charge measurements and an increased risk of problems from a build-up of static charge on the aircraft fuselage (which cannot be made entirely conductive as this would affect radio communication with the UAS). By mounting the charge sensors at a distance from the surface of the wings and encasing them in a conductive housing, the influence of any static charge that may build up during flight on the wings is also minimized. Using an entirely electric aircraft also removes any chance of charging the aircraft body from exhaust emissions. To minimize electrical noise from the aircraft systems, the power supply and logging of the charge sensors were completely decoupled from the rest of the aircraft. Another thing of importance to the quality of the charge measurements is the flight path of the UAS. Section 2c demonstrates the importance of roll velocity influence on the charge sensor measurements. Although this can be removed through developing a calibration method (as discussed in section 2d), it is also good practice to minimize the roll velocity to ensure that the sensor does not saturate. Here we employ a flight path that prioritizes long straight sections with minimal turns (and the turns are not included in the analysis of the final scientific measurements). Although the exact dependency of the movement of the UAS on the charge measurements (be it roll, yaw or pitch) will depend on the placement of the sensors on the aircraft, it is good practice to try to minimize the effect of such movements to minimize the complexity of correction method required. Proper tuning of the autopilot's flight control is also important, as it can greatly increase the stability of the UAS. As mentioned in section 2c, flying in straight sections minimizes the effect of the roll velocity on the measurements but does not completely delete it. This is particularly apparent when the UAS is flying within the ABL in convective conditions, and the autopilot makes corrections to the flight path to account for turbulent motions. Fig. 12 demonstrates the relationship between the roll velocity and charge sensor output voltage below the ABL (a) and above it (b). There is an approximately linear relationship between the two in both cases, but the gradient is steeper in the ABL (1.9 V m^{-1} s^{-1}) than above it (0.5 V m^{-1} s^{-1}). This is likely related to the aircraft's fuselage charging up more within the ABL than above it, which leads to an increased influence of the aircraft's motion on the charge sensors. A similar effect was reported by Hill (1982), who demonstrated that the gradient of the relationship between the bank angle of their UAS and E-field was steeper at 2000 ft than 6000 ft. Thus, flying above the ABL, rather than below it, is also advantageous to minimize the effects of aircraft movement on charge measurements. The correction method described in section 2d could be further improved by performing separate calibrations in and above the ABL.

Secondly, the flight past a metallic meteorological tower serves as a validation of the charge sensors and can be compared well with physical models. It enables investigating the behavior of the charge sensors on MASC-3 under controlled and reproducible conditions (section 3a). The results show excellent agreement between the space charge measured by the the sensor and the divergence of the E-field in the COMSOL simulation (Fig. 10). This shows that MASC-3 can reliably measure the space charge when the influence of the movement of the aircraft is removed.

Third, the first half of the diurnal cycle of a convective (fair weather) ABL is investigated, thus applying the measurement technique to a meteorological problem under realistic conditions (section 3b). The vertical profiles (Fig. 11) demonstrate the similarities between the space charge profiles and the meteorological profiles, which has been observed in other similar studies from balloons (e.g., Nicoll et al. 2018) and manned aircraft (Sagalyn and Faucher 1954). The magnitude of the space charge (up to 70 pC m^{-3}) is also comparable with balloon measurements of the same charge sensor as reported in Nicoll et al. (2018), which detected space charge of up to 100 pC m^{-3} in the ABL in fair weather conditions. This provides further evidence that the space charge measurements from the MASC-3 are responding to natural variations in the E-field.

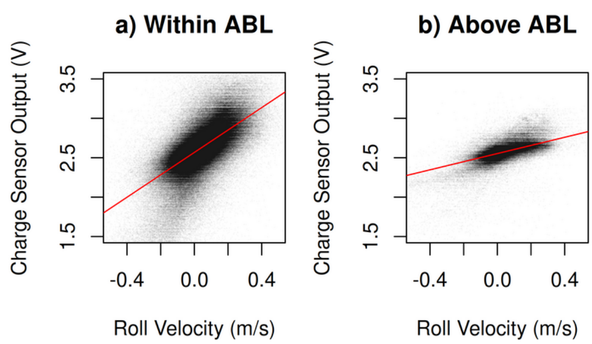

FIG. 12. a: Comparison of the different responses of the charge sensor to the roll velocity in the boundary layer (a) and above the boundary layer (b) in the free atmosphere. The data shown are composed of all measurement flights in which a clear inversion is identifiable as the upper limit of the ABL (flights 6,7,8,9,10,13). Note that the data shown contains the turns, as there is not enough rolling motion on the straight measurement sections to make a clear correlation discernible. The data is not corrected for roll velocity, and is timeshifted by 0.2 seconds to account for the timeshift in the charge sensor measurement (Fig. 5).

5. Conclusions

This study presents the first analysis of a new series of space charge and meteorology measurements made from a small unmanned aircraft platform. Charge measurements were made from wing-mounted probes using a 4 m wingspan fixed-wing UAS known as MASC-3. Flight data demonstrates a dependence of the charge sensor output on roll velocity of the UAS, which is corrected for using a series of calibration maneuvers during a calibration flight. A series of flights past a 99 m metal tower demonstrated excellent agreement between the charge sensor response and expected distortion in the E-field caused by the geometry of the mast, as modeled using the COMSOL electrostatic modeling software. Several vertical profile flights (up to 2.5 km) performed at different times during a fair-weather day characterized the evolution of the ABL. This demonstrated a close agreement between the space charge profiles and meteorological variables (particularly turbulence and boundary layer height), as would be expected on a fair-weather day with summertime convection.

The flight data discussed here supports the conclusion that it is possible to make sensible measurements of space charge in fair weather conditions from small unmanned aircraft, which are not significantly affected by the presence and movement of the aircraft. Further, this is possible with only a single small, inexpensive sensor and relatively straightforward data processing techniques. This contrasts with the E-field measurements from crewed aircraft discussed in the literature, which typically require many sensors and complex analysis techniques to derive accurate measurements of fair weather E-fields. Due to the increasing use of UAS in atmospheric science, this is an important finding, which may drive forward an increase in atmospheric electricity measurements from such platforms, and will help characterize and study the ABL and aerosol processes, including the transport of dust and volcanic ash layers. Additionally, further research into developing small and light E-field sensors is worth pursuing, since this would allow the E-field to be measured directly with small UAS.

Acknowledgments. We thank the following people for their support for the work: the pilot of MASC-3, Henrik Rieth; colleagues in the Environmental Physics Workgroup of the University of Tübingen, Jakob Boventer, Ines Weber, and Kjell zum Berge, who maintained MASC-3, provided the logistics and legal framework for the measurement flights and provided valuable support during the interpretation of the results.;

Frank Beyrich and the German Meteorological Service (DWD) for providing the infrastructure at the MOL-RAO and the invaluable support during and after the measurements.

The measurements in Falkenberg, which provided the data basis for this paper, were performed as a supplement to a Lidar validation flight project funded by the German Meteorological Service (DWD) under the funding code 4819EMF01 (VALUAS).

KAN acknowledges a NERC Independent Research Fellowship (NE/L011514/1) and (NE/L011514/2).

Data availability statement. The data that support the findings of this study are available from the corresponding author, Martin Schön, upon reasonable request.

APPENDIX

Supplementary Information

a. Calculation of turbulent kinetic energy

To obtain a vertical profile of the ABL, MASC-3 flies a series of measurement sections at a constant rate of climb from the ground to beyond the capping inversion of the ABL (Fig. 4). From these measurement sections, the temperature and humidity measurements are plotted as vertical profiles (Fig. 11a).

As a measure of turbulent fluctuations, the turbulent kinetic energy k is calculated for each measurement section (Fig. 11). Since the measurement sections are not horizontal but slant (from altitudes z_1 to z_2, Fig. 4), k (equation A1) is representative not only for a particular height but for a volume defined by z_1, z_2, and the length of the slant flight section above ground. For the flights presented here, $z_2 - z_1$ is around 10 % of the ABL height z_i. By ensuring the duration of each measurement section is longer than the integral time scale $\mathcal{T}$ of the wind components u, v and w, the measured volume includes the largest vortices present in the ABL (Stull 2015; Bange et al. 2013, 2002). For all measurement sections presented here, $\mathcal{T}$ is lower than 9 s, while the duration of each measurement section is around 50 s.

$$k = 0.5 \cdot \left(\overline{\mathrm{u}'^2} + \overline{\mathrm{v}'^2} + \overline{\mathrm{w}'^2} \right) \tag{A1}$$

References

Bange, J., F. Beyrich, and D. A. M. Engelbart, 2002: Airborne measurements of turbulent fluxes during litfass-98: Comparison with ground measurements and remote sensing in a case study. *Theor. Appl. Climatol.*, **73 (1)**, 35–51, https://doi.org/https://doi.org/10.1007/s00704-002-0692-6.

Bange, J., and Coauthors, 2013: Measurement of aircraft state, thermodynamic and dynamic variables. *Airborne measurements for environmental research: methods and instruments*, John Wiley and Sons.

Bateman, M. G., and Coauthors, 2007: A low-noise, microprocessor-controlled, internally digitizing rotating-vane electric field mill for airborne platforms. *J. Atmos. Oceanic Technol.*, **24 (7)**, 1245–1255, https://doi.org/https://doi.org/10.1175/jtech2039.1.

Clark, J. F., 1957: Airborne measurement of atmospheric potential gradient. *J. Geophys. Res.*, **62 (4)**, 617–628, https://doi.org/https://doi.org/10.1029/jz062i004p00617.

Clark, J. F., 1958: The fair-weather atmospheric electrical potential and its gradient. *Recent advances in atmospheric electricity*, L. G. Smith, Ed., Pergamon, 61–73.

COMSOL, 2021: COMSOL: Multiphysics Software for Optimizing Designs. Accessed 12 November 2021, https://uk.comsol.com/.

Gish, O. H., 1944: Evaluation and interpretation of the columnar resistance of the atmosphere. *Terrestrial Magnetism and Atmospheric Electricity*, **49 (3)**, 159–168, https://doi.org/https://doi.org/10.1029/TE049i003p00159.

Gish, O. H., and G. R. Wait, 1950: Thunderstorms and the earth's general electrification. *J. Geophys. Res.*, **55 (4)**, 473–484, https://doi.org/https://doi.org/10.1029/jz055i004p00473.

Gringel, W., and R. Muhleisen, 1978: Sahara dust concentration on the troposphere over the north atlantic derived from measurements of air conductivity. *Contrib. Atmos. Phys.*, **51**, 121–128.

Guido, R. C., 2016: A tutorial on signal energy and its applications. *Neurocomputing*, **179**, 264–282, https://doi.org/https://doi.org/10.1016/j.neucom.2015.12.012.

Gunn, R., 1947: The electrical charge on precipitation at various altitudes and its relation to thunderstorms. *Phys. Rev.*, **71 (3)**, 181, https://doi.org/https://doi.org/10.1103/physrev.71.181.

Gunn, R., 1948: Electric field intensity inside of natural clouds. *J. Appl. Phys. (Melville, NY, U. S.)*, **19 (5)**, 481–484, https://doi.org/https://doi.org/10.1063/1.1698159.

Harrison, R. G., K. A. Nicoll, Z. Ulanowski, and T. A. Mather, 2010: Self-charging of the eyjafjallajökull volcanic ash plume. *Environmental Research Letters*, **5 (2)**, 024 004.

Harrison, R. G., and Coauthors, 2021: Demonstration of a remotely piloted atmospheric measurement and charge release platform for geoengineering. *J. Atmos. Oceanic Technol.*, **38 (1)**, 63–75, https://doi.org/https://doi.org/10.1175/jtech-d-20-0092.1.

Hill, M. L., 1972: Introducing the electrostatic autopilot. *AIAA J.*, **10 (11)**, 22.

Hill, M. L., 1982: Influence of meteorological processes on the verticality of electric fields. Tech. Rep. ADA111549, John Hopkins University Applied Physics Lab, 16 pp. https://doi.org/https://doi.org/10.21236/ada111549.

Holt, C. C., 2004: Forecasting seasonals and trends by exponentially weighted moving averages. *International Journal of Forecasting*, **20 (1)**, 5–10, https://doi.org/https://doi.org/10.1016/j.ijforecast.2003.09.015.

Hoppel, W., R. V. Anderson, and J. C. Willet, 1986: Atmospheric electricity in the planetary boundary layer. *The Earth's Electrical Environment*, E. P. Krider, and R. G. Roble, Eds., The National Academies Press, 149 – 165, https://doi.org/10.17226/898.

Koshak, W. J., J. Bailey, H. J. Christian, and D. M. Mach, 1994: Aircraft electric field measurements: Calibration and ambient field retrieval. *J. Geophys. Res.: Atmos.*, **99 (D11)**, 22 781–22 792, https://doi.org/https://doi.org/10.1029/94jd01682.

Laroche, P., 1986: Airborne measurements of electrical atmospheric field produced by convective clouds. *Rev. Phys. Appl.*, **21 (12)**, 809–815, https://doi.org/https://doi.org/10.1051/rphysap:019860021012080900.

Mach, D. M., 2015: Technique for reducing the effects of nonlinear terms on electric field measurements of electric field sensor arrays on aircraft platforms. *J. Atmos. Oceanic Technol.*, **32 (5)**, 993–1003, https://doi.org/https://doi.org/10.1175/jtech-d-14-00029.1.

Mach, D. M., and W. J. Koshak, 2007: General matrix inversion technique for the calibration of electric field sensor arrays on aircraft platforms. *J. Atmos. Oceanic Technol.*, **24 (9)**, 1576–1587, https://doi.org/https://doi.org/10.1175/jtech2080.1.

Markson, R., and C. Price, 1999: Ionospheric potential as a proxy index for global temperature. *Atmos. Res.*, **51 (3-4)**, 309–314, https://doi.org/https://doi.org/10.1016/s0169-8095(99)00015-0.

Markson, R., J. Sedláček, and C. W. Fairall, 1981: Turbulent transport of electric charge in the marine atmospheric boundary layer. *J. Geophys. Res.: Oceans*, **86 (C12)**, 12 115–12 121, https://doi.org/https://doi.org/10.1029/jc086ic12p12115.

Mauz, M., A. Rautenberg, A. Platis, M. Cormier, and J. Bange, 2019: First identification and quantification of detached-tip vortices behind a wind energy converter using fixed-wing unmanned aircraft system. *Wind Energy Science*, **4 (3)**, 451–463, https://doi.org/https://doi.org/10.5194/wes-4-451-2019.

Mazur, V., L. H. Ruhnke, and T. Rudolph, 1987: Effect of E-field mill location on accuracy of electric field measurements with instrumented airplane. *J. Geophys. Res.: Atmos.*, **92 (D10)**, 12 013–12 019, https://doi.org/https://doi.org/10.1029/jd092id10p12013.

Nicoll, K. A., 2013: A self-calibrating electrometer for atmospheric charge measurements from a balloon platform. *Rev. Sci. Instrum*, **84 (9)**, 096 107, https://doi.org/https://doi.org/10.1063/1.4821500.

Nicoll, K. A., and R. G. Harrison, 2009: A lightweight balloon-carried cloud charge sensor. *Rev. Sci. Instrum.*, **80 (1)**, 014 501, https://doi.org/https://doi.org/10.1063/1.3065090.

Nicoll, K. A., and R. G. Harrison, 2016: Stratiform cloud electrification: comparison of theory with multiple in-cloud measurements. *Quart. J. Roy. Meteor. Soc.*, **142 (700)**, 2679–2691.

Nicoll, K. A., R. G. Harrison, H. G. Silva, R. Salgado, M. Melgao, and D. Bortoli, 2018: Electrical sensing of the dynamical structure of the planetary boundary layer. *Atmos. Res.*, **202**, 81–95, https://doi.org/https://doi.org/10.1016/j.atmosres.2017.11.009.

Nicoll, K. A., R. G. Harrison, and Z. Ulanowski, 2010: Observations of saharan dust layer electrification. *Environmental Research Letters*, **6 (1)**, 014 001.

Pinto, J. O., and Coauthors, 2021: The status and future of small uncrewed aircraft systems (UAS) in operational meteorology. *Amer. Meteor. Soc.*, **102 (11)**, E2121–E2136, https://doi.org/https://doi.org/10.1175/BAMS-D-20-0138.1.

Rautenberg, A., and Coauthors, 2019: The multi-purpose airborne sensor carrier MASC-3 for wind and turbulence measurements in the atmospheric boundary layer. *Sensors*, **19 (10)**, 2292, https://doi.org/10.3390/s19102292.

Rycroft, M. J., K. A. Nicoll, K. A. Aplin, and R. G. Harrison, 2012: Recent advances in global electric circuit coupling between the space environment and the troposphere. *J. Atmos. Terr. Phys.*, **90-91**, 198—-211, https://doi.org/https://doi.org/10.1016/j.jastp.2012.03.015.

Sagalyn, R. C., and G. A. Faucher, 1954: Aircraft investigation of the large ion content and conductivity of the atmosphere and their relation to meteorological factors. *J. Atmos. Terr. Phys.*, **5 (1-6)**, 253–272, https://doi.org/https://doi.org/10.1016/0021-9169(54)90046-x.

Stull, R., 2015: Turbulence Kinetic Energy. *Practical meteorology: an algebra-based survey of atmospheric science*, John Wiley and Sons, 708.

Tuma, J., 1899: Beiträge zur Kenntniss der atmosphärischen Elektricität III. Luftelektricitäts-Messungen im Luftballon. *Sitzungsber. Akad. Wiss. Wien, Math.-Naturwiss. Kl., Abt. 2A*, **108 (23 - 24)**, 227–260.

Wildmann, N., M. Hofsäß, F. Weimer, A. Joos, and J. Bange, 2014a: Masc–a small remotely piloted aircraft (rpa) for wind energy research. *Advances in Science and Research*, **11 (1)**, 55–61, https://doi.org/https://doi.org/10.5194/asr-11-55-2014.

Wildmann, N., M. Mauz, and J. Bange, 2013: Two fast temperature sensors for probing of the atmospheric boundary layer using small remotely piloted aircraft (RPA). *Atmos. Meas. Tech.*, **6 (2)**, https://doi.org/https://doi.org/10.5194/amt-6-2101-2013.

Wildmann, N., S. Ravi, and J. Bange, 2014b: Towards higher accuracy and better frequency response with standard multi-hole probes in turbulence measurement with remotely piloted aircraft (RPA). *Atmos. Meas. Tech.*, **7 (4)**, 1027–1041, https://doi.org/https://doi.org/10.5194/amt-7-1027-2014.

Williams, E. R., 2009: The global electrical circuit: A review. *Atmos. Res.*, **91 (2-4)**, 140–152, https://doi.org/https://doi.org/10.1063/1.43893.

Wilson, C. T. R., 1921: Investigations on lighting discharges and on the electric field of thunderstorms. *Philosophical Transactions of the Royal Society of London. Series A, Containing Papers of a Mathematical or Physical Character*, **221 (582-593)**, 73–115, https://doi.org/https://doi.org/10.1098/rsta.1921.0003.

Winn, W. P., 1993: Aircraft measurement of electric field: Self-calibration. *J. Geophys. Res.: Atmos.*, **98 (D4)**, 7351–7365, https://doi.org/https://doi.org/10.1029/93jd00165.

Zhang, Y., E. Duff, A. Agundes, B. Yeik, and K. L. Cummins, 2016: Small UAV airborne electric field measurements. *24th International Lightning Detection Conference & 6th International Lightning Meteorology Conference, San Diego, California*, San Diego, California, Vaisala, 1–7.